International Journal of Heat and Mass Transfer 52 (2009) 431–441

Contents lists available at ScienceDirect

International Journal of Heat and Mass Transfer

journal homepage: www.elsevier.com/locate/ijhmt

Experimental study on spreading and evaporation of inkjet printed pico-liter droplet on a heated substrate

Taewoong Lim [a], Sewoon Han [a], Jaewon Chung [a,*], Jin Taek Chung [a], Seunghwan Ko [b], Costas P. Grigoropoulos [b]

[a] Department of Mechanical Engineering, Korea University, 1 Anam-Dong 5 Ga, Sungbuk-Gu, Seoul 136-716, South Korea
[b] Laser Thermal Laboratory, Department of Mechanical Engineering, University of California, Berkeley, CA, USA

ARTICLE INFO

Article history:
Received 1 May 2007
Received in revised form 1 February 2008
Available online 3 August 2008

Keywords:
Flexible electronics
Inkjet
Droplet
Spreading
Evaporation

ABSTRACT

In this work, the spreading and evaporation of 2–70 pL droplet (17–50 μm diameter) of water and ethylene glycol jetted by drop-on-demand piezo-driven jetting head on the heated substrate are studied. According to the experimental results, the interfacial oscillation phenomena of water droplet whose Ohnesorge number (Oh) is about 10^{-2} is similar to that in inviscid impact driven region, while that of ethylene glycol droplet ($Oh \approx 10^{-1}$) is similar to that in highly viscous impact driven region followed by capillary driven extra spreading. In addition, various time scales used for nano/micro-liter droplets agree well with the times for interfacial oscillation, viscous damping, extra wetting, and evaporation in pico-liter droplets. In the case of water droplet, the spreading processes end before the evaporation becomes significant. However, in the case of highly viscous ethylene glycol droplet, the extra wetting overlaps the evaporation at high temperature.

1. Introduction

1.1. Objective

The impact of a droplet on a solid surface and the subsequent spreading and evaporation phenomena have been studied extensively, not only because of the fundamental interest in hydrodynamics, but also its practical importance in many industrial processes, including spray coating, inkjet printing, solder jetting, etc. Among them, the interest for inkjet printing has been growing recently due to its potential to be adapted to non-graphical applications such as the color filter deposition process for liquid crystal displays and the direct patterning of various functional materials for flexible plastic electronics as well as printed circuit boards, etc.

While the material in a typical graphical inkjet printing process is deposited via ink absorption into the paper, the printing material in the non-graphical application is deposited on the substrate mainly by ink evaporation. Therefore, understanding the evaporation phenomena of pico-liter droplets is important in non-graphical applications. For example, when multiple droplets are inkjetted at the same spot to increase the thickness of deposited material while keeping the pattern width minimum, the next droplet should impact after the evaporation of the previous droplet is complete. Therefore, the jetting sequence of multiple nozzles should be designed so that the jetting interval on the same spot is longer than the evaporation time. In addition, the droplet spreading after impact on the substrate is closely related not only to the minimum printing resolution, but also to the evaporation process, since the evaporation rate is directly proportional to the interfacial area. While the spreading and evaporation of nano/micro-liter droplets (greater than 500 μm diameter) have been studied extensively in the past [1,2], very few studies have been reported on pico-liter droplets (smaller than 100 μm diameter) [3].

Our objective in this paper is to report the spreading and evaporation phenomena of 2–70 pL droplet (i.e. 17–50 μm diameter) of water and ethylene glycol and explain the observed phenomena. The last objective is carried out by applying time scale analysis provided for nano/micro-liter droplet. In addition, the effect of the droplet size, the substrate temperature and the different fluids on spreading and evaporation phenomena are studied with purpose of improving both printing resolution and speed.

1.2. Review of impact regimes and time scales for spreading and evaporation phenomena

The initial spreading dynamics after impact is characterized mainly by the Ohnesorge number (Oh) and Weber number (We) that are

$$Oh = \frac{\mu}{\sqrt{\rho\sigma D_0}}, \tag{1}$$

$$We = \frac{\rho D_0 U_0^2}{\sigma} = (Oh\,Re)^2, \tag{2}$$

* Corresponding author. Tel.: +82 2 3290 3374; fax: +82 2 926 9290.
E-mail address: jwon@korea.ac.kr (J. Chung).

0017-9310/$ - see front matter © 2008 Elsevier Ltd. All rights reserved.
doi:10.1016/j.ijheatmasstransfer.2008.05.028

Nomenclature

A_{lv}	liquid and vapor interface area (m^2)
Bo	bond number
C	vapor concentration (kg/m^3)
Ca	capillary number
D	droplet contact diameter (m)
D_0	droplet diameter before impact (m)
Δ	vapor diffusion coefficient (m^2/s)
g	gravitational constant (9.81 m/s^2)
h	droplet height (m)
Oh	Ohnesorge number
R	contact radius (m)
R_0	droplet radius before impact (m)
r	radial distance (m)
r	radius of curvature (m)
Re	Reynolds number
T	temperature (°C)
t	time (s)
u	moving velocity of substrate (m/s)
U_0	velocity of droplet before impact (m/s)
V	droplet volume (L)
We	Weber number
β	spreading ratio
γ	interfacial tension (N/m)
θ	contact angle (rad)
κ	constant, 0.0138 given by Hoffman
μ	viscosity (N s/m)
ρ	density (kg/m^3)
σ	surface tension (N/m)
τ	time scale

Subscripts

0	before impact
adv	advancing
amp	amplitude
cond	thermal conduction
damp	damping
dyn	dynamic
eq	equilibrium
evap	evaporation
f	fluid
fit	fitting
kin	kinetic
lv	liquid and vapor
max	maximum
osc	oscillation
rec	receding
sat	saturation
s	substrate
visc	viscous
wet	wetting
∞	ambient

where ρ is the fluid density, D_0 and U_0 are the diameter and velocity of the droplet before impact, respectively; μ is the viscosity, and σ is the surface tension. Here, Oh represents the ratio of the time scale of the interfacial oscillation period, $\tau_{osc} = \sqrt{\rho D_0^3/\sigma}$ to the viscous damping time, $\tau_{visc} = \rho D_0^2/\mu$ that represents the decay time scale of the interfacial oscillation. Therefore, a high Oh number means $\tau_{visc} \ll \tau_{osc}$, so that interfacial oscillation is overdamped. Note that τ_{osc} also represents the time scale for surface tension driven wetting for inviscid fluid. In addition, the time scale for the surface tension driven wetting for highly viscous fluid is expressed as $\tau_{wet} = \mu D_0/\sigma$ [4], in which case the Oh number is the root of τ_{wet}/τ_{visc}. Similarly, the Weber number can be considered as the square of the ratio of the kinematic spreading time scale, $\tau_{kin}(=D_0/U_0)$ and the time scale of surface tension driven wetting resisted by inertia, τ_{osc}. Compared to the above time scales, evaporation occurs slowly and is mainly dominated by the vapor diffusion process. Hence, the evaporation time scale can be expressed as $\tau_{evap} \approx \rho D_0^2/\mathscr{D}C_{sat}$, where Δ and C_{sat} are the vapor diffusion coefficient and the saturated vapor concentration, respectively. The above-mentioned time scales and dimensionless numbers are summarized in Table 1.

Table 1
Time scales and dimensionless number related to droplet spreading and evaporation phenomena

	Time scale		
Kinetic	$\tau_{kin} \approx D_0/U_0$	Ohnesorge number	$Oh = \frac{\tau_{osc}}{\tau_{vis}} = \sqrt{\frac{\tau_{wet}}{\tau_{vis}}} = \frac{\tau_{wet}}{\tau_{osc}}$
Oscillation[a]	$\tau_{osc} \approx \sqrt{\rho D_0^3/\sigma}$		
Viscous damping	$\tau_{vis} \approx \rho D_0^2/\mu$	Weber number	$We = \left(\frac{\tau_{osc}}{\tau_{kin}}\right)^2$
Wetting[b]	$\tau_{wet} \approx \mu D_0/\sigma$		
Evaporation	$\tau_{evap} \approx \rho D_0^2/\mathscr{D}C_{sat}$	Reynolds number	$Re = \tau_{vis}/\tau_{kin}$

[a] Also time scale for surface tension driven wetting resisted by inertia
[b] Can be interpreted as surface tension driven wetting resisted by viscosity

Based on these dimensionless numbers, Schiaffino and Sonin [1] distinguished four impact regimes, such as inviscid, impact-driven region (I), inviscid, capillary driven region (II), highly viscous, capillarity-driven region (III) and highly viscous, impact-driven region (IV) as shown in Fig. 1. In all regimes, the final droplet shape is determined by the surface tension and the contact angle. When the four regimes in Fig. 1 are divided by assuming Oh and We to unity, the current experimental data belong to regime I. However, on the basis of experimental results [1], it was shown that the actual transition between the inviscid and viscous regimes occurred at Oh number of 10^{-2}–10^{-1} which is also verified in the present work. Therefore, the current experimental data of ethylene glycol belong to regime IV (impact driven, viscous) and those of water are located in the transition regime.

The evolution of the droplet impact and spreading process in regime I can be divided into four phases as (i) the kinematic phase, (ii) the spreading phase, (iii) the relaxation phase, and (iv) the wetting/equilibrium phase [2]. During the kinematic phase, the inertia is dominant in the course of impact, so that the droplet has a truncated spherical shape and the spreading ratio, β, increases according to a power law in time as shown in Eq. (3).

$$\beta = 2.9\sqrt{t/\tau_{kin}} \quad \text{when } 0 < t/\tau_{kin} < 0.1 \tag{3}$$

In the following spreading phase, the lamella is ejected from the base of the droplet and the dynamic pressure of the impact drives the spreading in competition with inertia. During this phase, the velocity of the contact line (i.e. capillary number) is relatively high, so the dynamic advancing contact angle, $\theta_{dyn,adv}$, is bigger than the equilibrium advancing contact angle, $\theta_{eq,adv}$. When the equilibrium receding contact angle, $\theta_{eq,rec}$, is not small, the spreading often overshoots the spherical cap that can be formed at equilibrium conditions with $\theta_{eq,rec}$ and therefore the spreading diameter is maximized. The maximum spreading ratio, β_{max}, and the time for the maximum spreading, (≈ 1–$5\tau_{kin}$) were

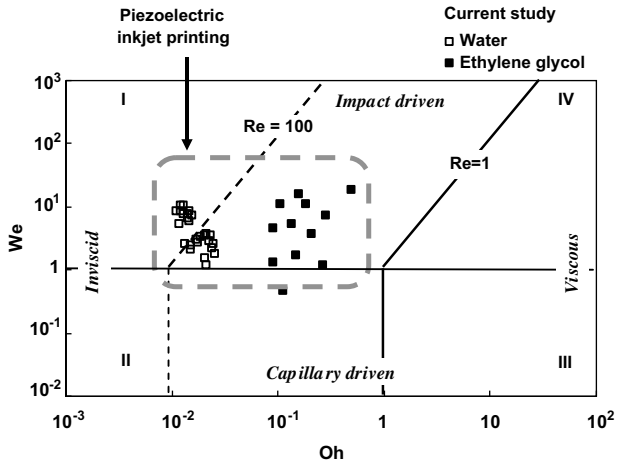

Fig. 1. Impact regime map.

predicted theoretically in many studies balancing the initial kinetic and surface energies of the incoming droplet with the transient kinetic and surface energy of the spreading film and the viscous dissipation [5–11]. Therefore, β_{max} mainly depends on both *We* and *Oh,* while only a few correlations include the effect of the dynamic contact angle, which is important for the prediction of β_{max}. It is noted that the evaluation of the energy of spreading droplet and the viscous dissipation requires a certain assumed velocity profile leading to significant error. Nonetheless, these models predict β_{max}relatively well, when $We > 100$ so that $\beta_{max} > 2–3$.

In the relaxation phase, the interface oscillation is damped out by viscous dissipation and the spreading diameter often recedes. The surface tension and the receding contact angle become significant in this phase. When the fluid perfectly wets the surface, only interfacial oscillation could be present and the receding phenomenon would be absent. After this phase, the wetting or equilibrium phase follows, so that spreading may continue when the fluid perfectly wets the surface or the spherical cap of the droplet shape does not change until the droplet volume decreases due to evaporation.

2. Experimental setup

2.1. Drop-on-demand printing and image capturing system

Pico-liter droplets of a pure fluid are dispensed with velocity of few m/s using the drop-on-demand (DOD) printing system (Fig. 2). The DOD jetting system is composed of a backpressure control system, a piezo-electrically driven jetting head and electrical signal generation systems [12]. MicroFab's piezo-jet heads with 10 and 30 μm of nozzle diameters were used to produce pico-liter droplets. The arbitrary function generator generates the bipolar voltage waveform with the same positive and negative amplitudes (about ±2 V) and with 40 μs dwell time. This bipolar voltage waveform is amplified about five to ten times, and drives the piezo-jet head to eject a pico-liter droplet. The impact velocity (U_0) is controlled by changing the amplified voltage amplitude and the dwell time, whose effect on the droplet generation was discussed in the earlier publication [12]. The droplets are generated at the frequency of 10 Hz and a precision translation stage is moved at 2–3 mm/s to observe the spreading and evaporation of a single droplet. The temperature of the substrate is controlled within ±4 °C by a thermocouple and a mica heater. Vacuum suction (300 mbar) is applied through 0.5 mm diameter holes to hold the silicon substrate for better thermal contact. The printing system is installed in clean room (Class 1000) and ambient temperature and relative humidity are controlled within 25 ± 2 °C and 45 ± 5%, respectively. The same arbitrary function generator used to drive the piezo-jet head also drives a light-emitting diode (LED) so that the sequential cross-sectional images of the droplet spreading and evaporation are obtained by changing the delay time between droplet generation and LED backlight. To obtain the images of the flying or fast oscillating pico-liter droplet, a strong illumination with short exposure time (several tens of microseconds) is required. For this reason, the voltage for LED is also amplified to 10–20 V, which is much higher than the burnout voltage of the LED under the continuous lightening condition.

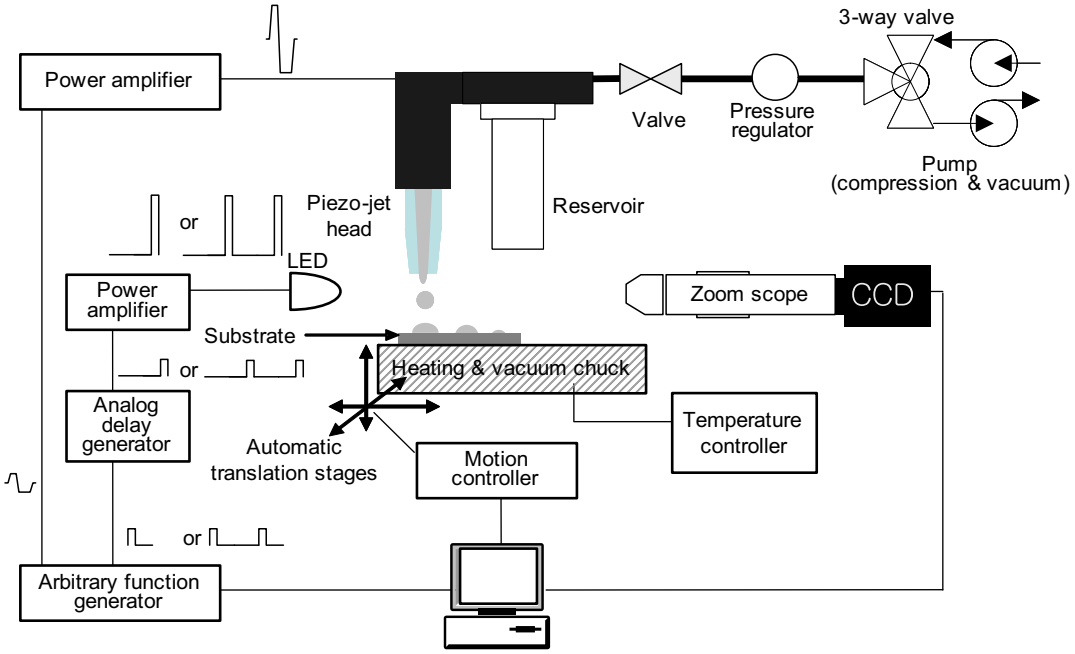

Fig. 2. Schematics of inkjet printing system and flash video microscopy system.

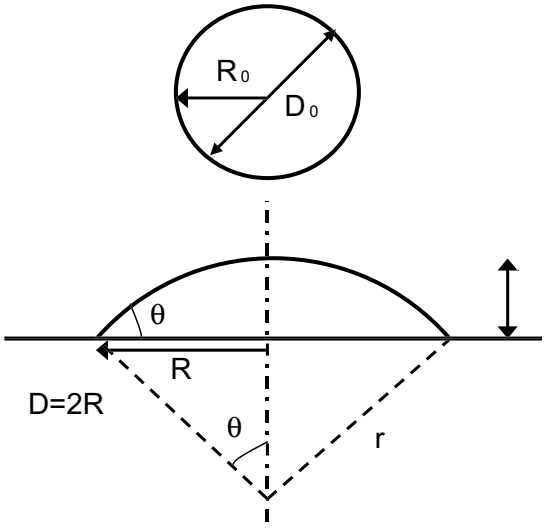

Fig. 3. Geometric parameters of the sessile droplet with spherical cap.

2.2. Geometric relationship of the sessile droplet with a spherical cap

When the oscillation of a liquid–vapor interface is damped out after impact (e.g. a few hundred microseconds from impact in the case of the pico-liter droplet), both the Bond number (Bo) and the capillary number (Ca) are small, so that the sessile droplet has the shape of a spherical cap. (Fig. 3) Therefore, the measurements of two geometric parameters among the radius of curvature (r), the contact radius (R), the height (h), and the contact angle (θ) of the sessile droplet enable calculation of the other parameters as well as the droplet volume (V) and the liquid and vapor interface area (A_{lv}) using Eqs. (4)–(7). In addition, the spreading ratio (β), which is the ratio of the contact diameter (D) to the droplet diameter before impact (D_0) can be expressed as a function of the contact angle in Eq. (8).

$$r = \frac{R}{\sin\theta} \tag{4}$$

$$h = \frac{R(1-\cos\theta)}{\sin\theta} \tag{5}$$

$$V = \frac{\pi}{3}h^2(3r-h) = \frac{\pi}{3}R^3\frac{(1-\cos\theta)(2+\cos\theta)}{\sin\theta(1+\cos\theta)} \tag{6}$$

$$A_{lv} = 2\pi rh = \frac{2\pi R^2}{1+\cos\theta} \tag{7}$$

$$\beta = \frac{D}{D_0} = \left(\frac{4\sin\theta(1+\cos\theta)}{(1-\cos\theta)(2+\cos\theta)}\right)^{1/3} \tag{8}$$

3. Droplet impact and spreading

In piezoelectric DOD inkjet printing, the fluid viscosity and the surface tension of a fluid should range 0.001–0.01 N s/m and 0.035–0.07 N/m, respectively [13]. In addition, the droplet diameter should be 10–100 μm for moderate resolution and the impact velocity should be 2–5 m/s to ensure sufficient ballistic accuracy. Based on these numbers, the orders of *We* and *Oh* for piezo-electric inkjet printing range from 1 to 10^2 and from 10^{-2} to 1, respectively. Our experimental results are also in this region as depicted in Fig. 1. Fig. 4(a) and (b) show time resolved images of the spreading and interface oscillation of water droplets at room temperature. Interface oscillation is evident up to about 100 μs due to relatively small viscous damping. In addition, a weak spreading oscillation is observed due to the underdamped interfacial oscillation and the contact angle hysteresis. In detail, the interfacial oscillation due to relatively small viscous damping results in the concave interface at the contact line (e.g. 35 and 65 μs images in Fig. 4(a)). When the apparent contact angle at the contact line is smaller than the equilibrium receding contact angle ($\theta_{eq,rec}$), the contact line can recede, which results in the spreading oscillation. Evaporation during the relaxation phase is negligible, and therefore, the volume calculated from the sessile droplet matches well with the droplet volume before impact. Note that the strong spreading overshoot is not desirable for achieving enhanced inkjet printing resolution. The oscillation period ($\tau_{osc,fit}$) and damping time ($\tau_{damp,fit}$) are obtained by fitting the following equations to the measured data of the contact radius (R) and height (h).

$$R(t) = R_{eq} + R_{amp}\,e^{-t/\tau_{damp,fit}}\sin\left(2\pi(t-\tau_1)/\tau_{osc,fit}\right) \tag{9}$$

$$h(t) = h_{eq} + h_{amp}\,e^{-t/\tau_{damp,fit}}\sin\left(2\pi(t-\tau_2)/\tau_{osc,fit}\right) \tag{10}$$

Here, R_{eq} and h_{eq} represent the contact radius and height after the oscillation disappears. The same $\tau_{osc,fit}$ and $\tau_{damp,fit}$ of the exponential decay function are used to fit the measured height and contact radius data, while the oscillation amplitudes (R_{amp} and h_{amp}) and the lagging times (τ_1 and τ_2) are determined by fitting the respective experimental data. According to the fitting results, the oscillation periods of Fig. 4(a) and (b) are about 31 and 22 μs, respectively, which are in the same order of magnitude with the calculated oscillation periods (39 and 36 μs) obtained from the equation for τ_{osc} in Table 1. In addition, the damping time of Fig. 4(a) and (b) are about 42 and 56 μs, respectively, which corresponds to about $(0.016 \sim 0.018)\tau_{vis}$ (based on τ_{vis} Table 1). Schiaffino and Sonin [1] proposed $0.008\tau_{vis}$ for the damping time by fitting the experimental results, which is consistent with our results. Considering the exponential decay of the oscillation amplitude, the time for the total relaxation phase can be scaled as 3–4 times of $0.017\tau_{vis}$. In the case of the ethylene glycol droplet (Fig. 5), only the height oscillates within one period and is then damped out due to high viscosity. The spreading oscillation is not observed in the case of ethylene glycol droplet, since the apparent contact angle at the contact line does not change significantly due to relatively high viscous damping and $\theta_{eq,\ rec}$ is relatively small. $\tau_{osc,fit}$ and $\tau_{damp,fit}$ used in the curve fitting are 23 μs ($0.66\tau_{osc}$) and 7 μs ($0.09\tau_{vis}$), respectively. It is noted that, however, the oscillation does not last even one period, so that these fitting results are not as accurate as those for water droplets.

Fig. 6 shows the experimental spreading ratio (β) of the water droplet after the interface oscillation disappears (i.e. after relaxation phase). The spreading ratio after the relaxation phase increases as the impact inertia (i.e. *We*) increases. The dotted lines represent the spreading ratios of truncated spheres calculated from Eq. (8) with the previously measured equilibrium advancing angle ($\theta_{eq,adv} = 60°$) and the receding contact angle ($\theta_{eq,rec} = 40°$). As for the printing resolution, the prediction of β after the relaxation phase is important. As mentioned above, most theoretical energy balance correlations for β that are valid for high *We*, result in overestimating the current experimental results ($0.5 < We < 20$). Fukai et al. [14] developed correlations for the maximum spreading ratio by fitting the coefficient from Chandra and Avedisian's correlation using the numerical simulation results.

$$\frac{We}{Re^{0.772}}\beta_{max}^4 + 4.58(1-\cos(\theta_{dyn}))\beta_{max}^2 - 1.5We - 8 = 0 \quad (5 < \mathrm{We} < 2720 \text{ and } 20 < \mathrm{Re} < 2900) \tag{11}$$

Since this correlation is valid for relatively low *We*, it is compared with the current experimental results. Here, β_{max} represents the maximum spreading ratio if the spreading oscillation occurs at high *We*. However, in the current conditions, the spreading oscillation is not strong, so that β_{max} approximately equals the spreading ratio, β

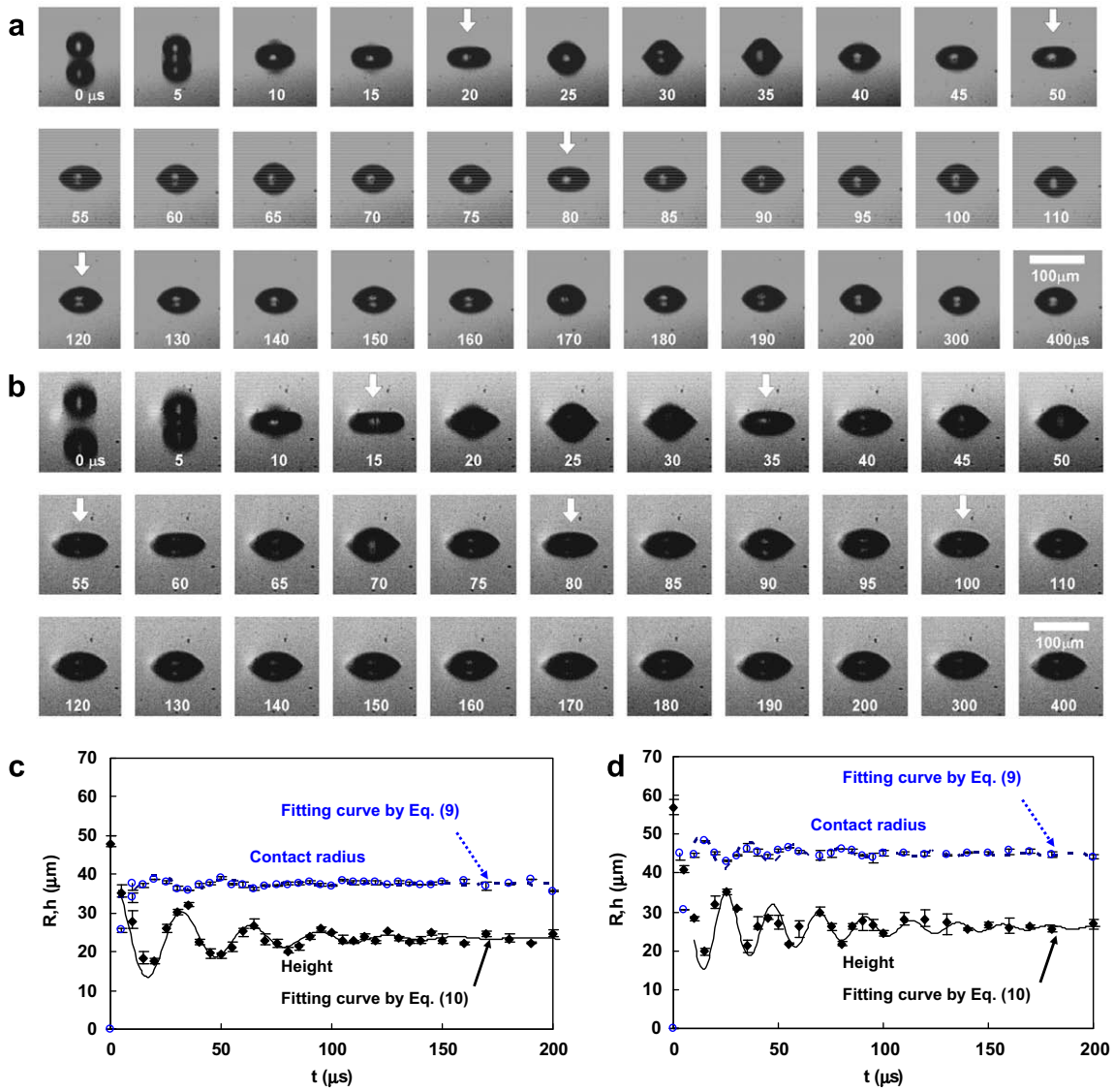

Fig. 4. Time resolved cross-sectional images of oscillating water droplet impacting on a silicon substrate at room temperature. The arrows indicate the sequences of droplet flattening during the interface oscillation. (a) The impact velocity and the diameter of the droplet are 1.9 m/s and 48.1 μm and the stabilized spreading ratio is 1.56 (Re = 107, Oh = 0.015, We = 2.4) (b) The impact velocity and the diameter of the droplet are 3.1 m/s and 45 μm and the stabilized spreading ratio is 1.59 (Re = 205, Oh = 0.013, We = 7.6). (c) The contact radius and the height of (a). The fitted parameters are τ_{osc} = 31 μs and τ_{damp} = 42 μs. (d) The contact radius and the height of (b). The fitted parameters are τ_{osc} = 22 μs and τ_{damp} = 56 μs.

after the relaxation phase. To calculate β_{max} from Eq. (11), the dynamic advancing contact angle, θ_{dyn}, should be calculated. θ_{dyn} at low Ca can be predicted by Hoffmann's correlation, which is most widespread [15],

$$\kappa(\theta_{dyn}^3 - \theta_{eq}^3) \cong Ca = \frac{\mu}{\sigma}\frac{dR}{dt}, \tag{12}$$

where θ_{eq} is an equilibrium contact angle and κ is a constant given by Hoffman to be about 0.0138. The dynamic contact angles calculated from Eq. (12) match well with those of the other models [16,17] when Ca is smaller than 0.3 as shown in Fig. 7. Here, the equilibrium advancing contact angle of 60° is used. Approximating the impact velocity as the velocity of the contact line, the capillary numbers in Fig. 4(a) and (b) are calculated as 0.023 and 0.037, respectively and the corresponding dynamic contact angle is about 90° from the Fig. 7 which is in good agreement with the images in Fig. 4(a) and (b). In addition, when the dynamic contact angle calculated from Hoffmann's correlation is used for θ_{dyn} in Eq. (12) instead of the constant 90° of θ_{adv}, the calculated β_{max} shows better agreement with the experimental results. This signifies that during the spreading phase the impact speed has significant influence on the dynamic contact angle, which also affects the maximum spreading ratio. However, the above correlation for the dynamic contact angle (Eq. (12)) can give only a rough estimation, since the inertia effect and the flow field of impacting droplet are not considered [18].

When the contact angle (θ) after the relaxation phase exceeds $\theta_{eq,adv}$, extra wetting should occur due to the capillary force imbalance at the contact line. This phenomenon can be clearly seen in droplets of highly viscous ethylene glycol, whose equilibrium contact angle is as small as 30°, as shown in Fig. 8. Extra wetting occurs in several milliseconds until θ approaches $\theta_{eq,adv}$ and the transient contact diameter during extra wetting matches well with theoretical predictions by Eq. (12) based on droplet volume conservation [1]. Therefore, the capillary force imbalance drives the extra wetting resisted mainly by viscosity. The extra wetting time scale (τ_{wet}) can be expressed as $\mu D_0/\sigma$, as mentioned previously. However, Hoffmann's correlation (Eq. (12)) suggests that the actual

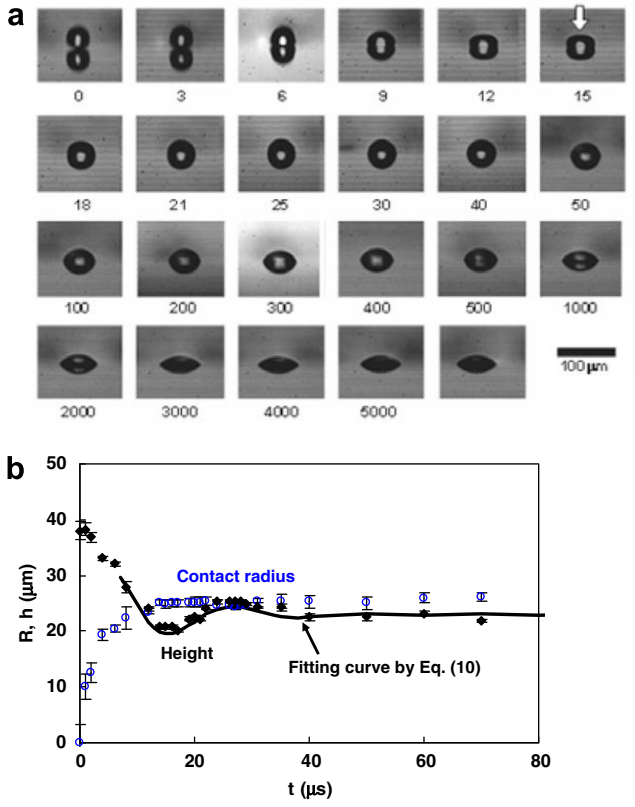

Fig. 5. (a) The time resolved cross-sectional image of oscillating ethylene glycol droplet after impact on a silicon substrate at a room temperature. The impact velocity and the diameter of the droplet are 1.8 m/s and 37.3 μm, respectively (Re = 3.7, Oh = 0.45, We = 2.8). The arrows indicate the sequences of the droplet flattening during the interface oscillation. (b) Time evolution of the contact radius and the height. The fitted parameters of the curve are τ_{osc} = 23 μs and τ_{damp} = 7 μs.

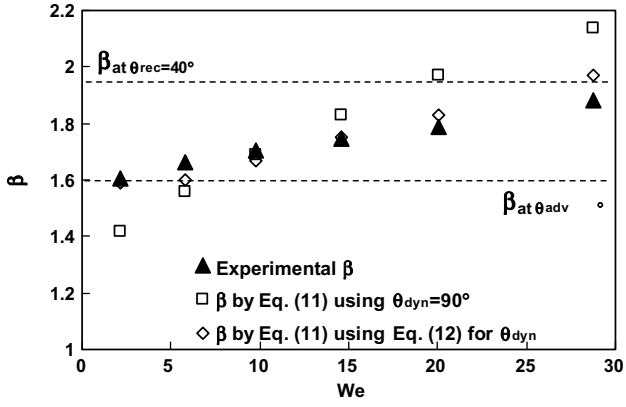

Fig. 6. The spreading ratio depending on the Weber number at room temperature.

contact line velocity and wetting time should be scaled as $\kappa\sigma/\mu$ and $(\mu D_0)/(\kappa\sigma)$, respectively. Note that the dimensionless wetting time in Fig. 8 is scaled by κ = 0.0138 and the extra wetting occurs from t_{wet}/κ = 0.1 to 1. The extra wetting after the relaxation phase is not observed for the water droplet. The wetting time scale of the water droplet for the case in Fig. 4 is calculated to about 40 μs, which is on the same order of the oscillation period. Therefore, if there had been significant imbalance of Young–Laplace force at the contact line, the extra wetting for the water droplet should have occurred during the relaxation phase. However, in the case of highly viscous ethylene glycol, the extra wetting is evident after

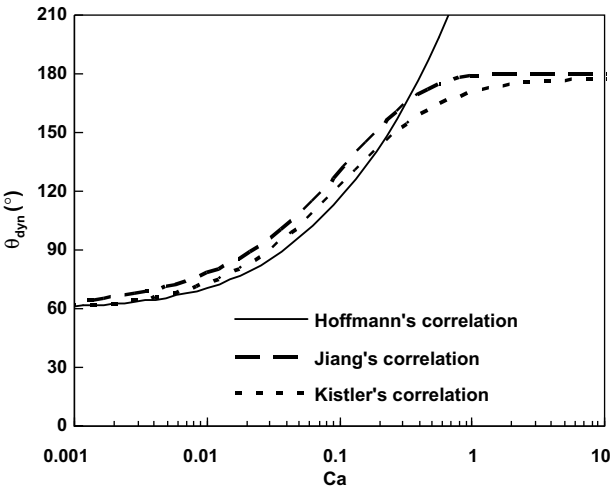

Fig. 7. Dynamic contact angle (θ_{dyn}) depending on the capillary number at 60° of the equilibrium contact angle (θ_{eq})

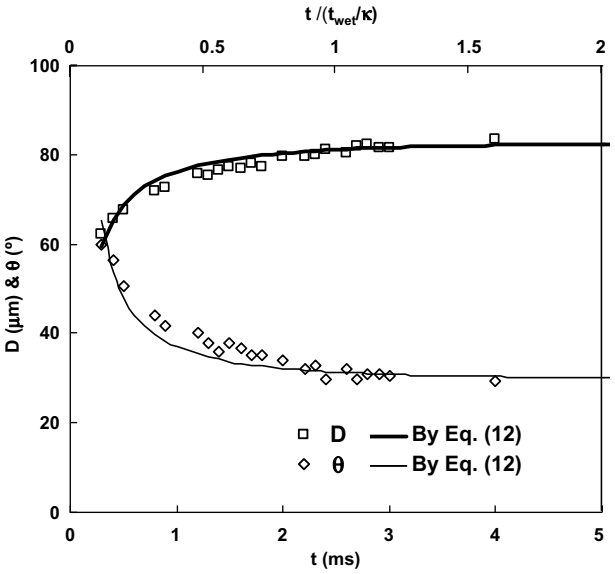

Fig. 8. Extra wetting of ethylene glycol droplet at room temperature after the relaxation phase. The droplet diameter before impact (D_0) and the impact velocity (U_0) are 38.5 μm and 4.7 m/s, respectively (Re = 10, Oh = 0.44, We = 20). The calculated droplet volume during the extra wetting phase is maintained at 30 pL within 7% error.

the relaxation phase, since the extra wetting time scale (≈1200 μs) is much larger than the oscillation period (≈35 μs).

4. Evaporation of sessile droplet

4.1. Evolution of contact diameter and contact angle during evaporation

The evaporation of the impacted sessile water and ethylene glycol droplets is observed by changing the temperature of the silicon substrates. Table 2 summarizes the experimental conditions for the droplet evaporation experiment. Fig. 9(a) shows the typical images of the evaporating water droplet (about 42 μm of droplet diameter) at various elapsed times after the relaxation phase. Note that the evaporation during the relaxation phase is negligible, since the total evaporation time (a few hundred milliseconds in Fig. 9) is

Table 2
Experimental conditions for the evaporation experiments

Case Number[a]	Droplet diameter, D_0 (μm)	Impact velocity U_0 (m/s)	Substrate temperature T_s (°C)	Jet head temperature (°C)	Re	Oh	We
W-10-30	18.1	2.67	30	23	52.4	0.025	1.77
W-10-40	17.8	3.22	40	24	64.5	0.025	2.56
W-10-50	19.2	3.59	50	26	80.4	0.023	3.43
W-10-70	18.2	3.31	70	29	73.8	0.023	2.78
W-10-90	18.7	2.11	90	32	51.2	0.021	1.17
W-10-110	17.0	2.51	110	36	59.6	0.021	1.51
W-10-130	18.1	3.23	130	43	92.2.	0.018	2.70
W-30-40	41.7	3.52	40	26	171.4	0.016	7.17
W-30-70	42.1	3.79	70	27	195.2	0.015	8.43
W-30-90	41.2	3.36	90	32	179.7	0.014	6.52
W-30-110	41.2	2.09	110	36	120.7	0.013	2.56
W-30-130	42.0	2.99	130	43	197.8	0.012	5.38
EG-30-80	38.1	2.81	80	30	9.38	0.285	7.16
EG-30-120	38.0	2.00	120	40	9.14	0.210	3.69
EG-30-160	38.3	1.34	160	52	8.85	0.147	1.70
EG-30-200	38.1	0.70	200	61	6.04	0.114	0.47
EG-30-220	35.6	1.19	220	71	12.46	0.092	1.30

[a] Case number represents the fluid used for jetting (W, water; EG, ethylene glycol), the nozzle diameter (10 or 30 μm) and the substrate temperature (°C) in order.

much longer than the relaxation time (a few hundred microseconds as shown in Fig. 4). The contact radius (R) and droplet height (h) are measured from the images in Fig. 9(a) and the other parameters such as the radius of curvature, contact angle and the droplet volume are calculated from Eqs. (4)–(8). The droplet volume before impact and that after relaxation phase (i.e. 200–300 μs after impact) match well within 5%. After the relaxation phase, the volume of sessile droplets decreases while the contact area remains pinned, so that only the contact angle decreases (Fig 9(b)). Then (after 100 ms), the contact area is depinned and the contact diameter decreases maintaining the receding contact angle at about 40°, which matches well with the measured equilibrium receding angle (37–42°) at room temperature. Note that a rough substrate surface can delay this depinning phenomenon, so that the contact angle can decrease below an equilibrium receding angle. Accordingly, in a rough surface, most of the evaporating droplet lifetime can be occupied by the first stage where the contact area remains pinned. As shown in Fig. 10, the evaporation rate of the water droplet increases with the substrate temperature until the droplet rebounce phenomenon (Leidenfrost phenomenon) occurs and the evaporation phase with constant contact area is followed by the evaporation phase with constant contact angle in the entire range of the substrate temperature. Note that the initial droplet volume

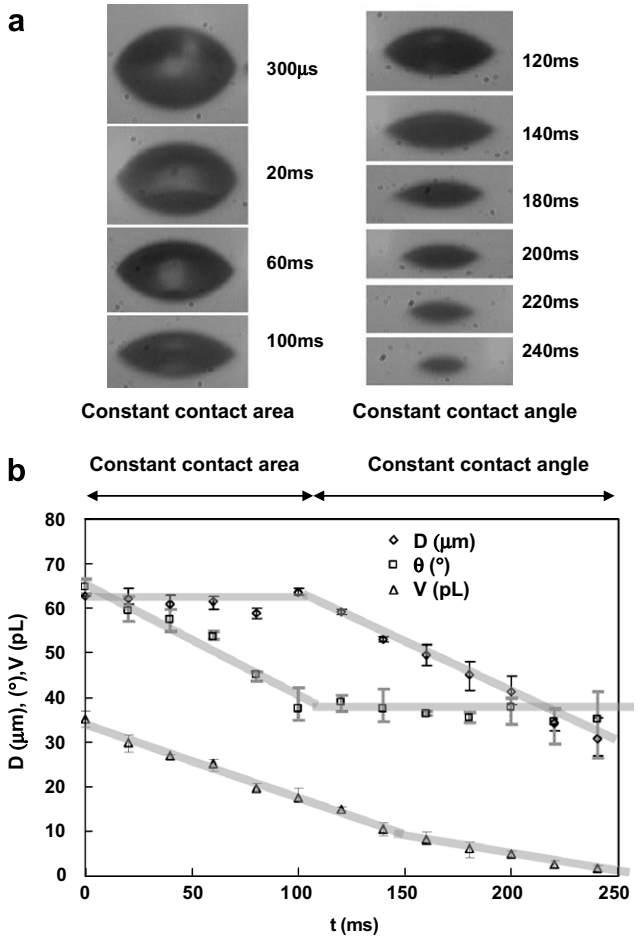

Fig. 9. Water droplet (D_0 = 42 μm) evaporating on a silicon substrate heated at 40 °C (W-30-40 in Table 3). (a) Droplet evaporation images. (b) Evolutions of contact diameter, contact angle and droplet volume.

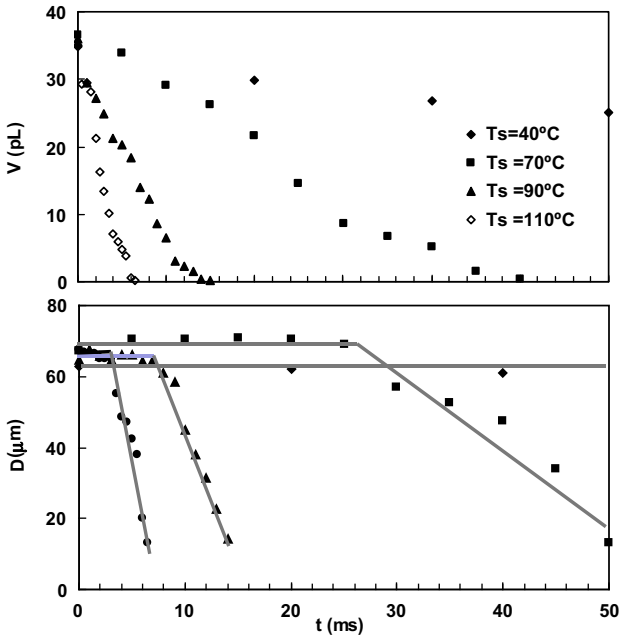

Fig. 10. The evolutions of droplet volume (V) and contact diameter (D) of the water droplet on a silicon substrate depending on the substrate temperature (T_s). The corresponding case numbers in Table 3 are W-30-40 ~110.

Table 3
Scaled time scale of droplet spreading and evaporation

	Scaled time scale	Water[a]	Ethylene glycol[b]
Kinetic phase	$0.1\tau_{kin}$	≈3 μs	≈2 μs
Spreading phase	$(1–2)\tau_{kin}$	≈ 25 μs	≈20 μs
Oscillation period	τ_{osc}	≈40 μs	≈40 μs
Viscous damping time	$0.015\tau_{vis}$	≈40 μs	≈ 2 μs
Extra wetting period	τ_{wet}/κ	≈40 μs	≈1 ms
Evaporation period	$0.2\tau_{evap}$	≈800 ms at 25 °C	
≈20 ms at 100 °C	≈500 ms at 100 °C		
≈10 ms at 200 °C			

[a] At T_s = 25 °C, U_0 = 2 m/s and D_0 = 48 μm.
[b] At T_s = 25 °C, U_0 = 2 m/s and D_0 = 39 μm.

and contact diameter vary for each case due to the different jetting conditions for stable droplet generation (Table 3). When the diameter (D_0) of the water droplet decreases to about 18 μm (Fig. 11), the total evaporation time decreases, but the evaporation rate decreases due to the smaller evaporation interfacial area. Here, the evaporation with constant contact area followed by the evaporation with constant contact angle is also observed over the entire substrate temperature range.

However, the evaporation of ethylene glycol droplet (about 38 μm of the droplet diameter) shows different trends depending on the substrate temperature. When the substrate temperature is lower than 120 °C (Fig. 12(a)), extra wetting is clearly observed after the relaxation phase while the droplet volume decreases. As mentioned, this extra wetting is due to the larger contact angle formed after the relaxation phase than the equilibrium advancing contact angle of ethylene glycol on silicon surface. However, the volume decreases due to evaporation, so that this extra wetting phase ends after several milliseconds and the contact area remains pinned up to about 35 ms as the contact angle decreases to about 40°. Finally, the contact diameter decreases at the constant receding contact angle of 40°. When the substrate temperature is elevated to 160 °C (Fig. 12(b)), extra wetting is not observed due to strong evaporation. Note that the receding angle of ethylene glycol at a high temperature (about 40° in Fig. 12) is even larger than

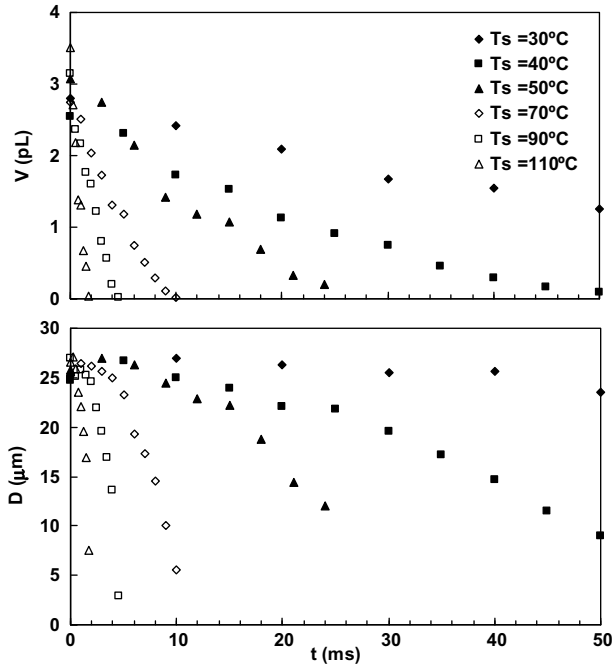

Fig. 11. The evolution of droplet volume (V) and contact diameter (D) of the evaporating water droplet on a silicon substrate depending on the substrate temperature (T_s). The corresponding case numbers in Table 3 are W-10-30 ~110.

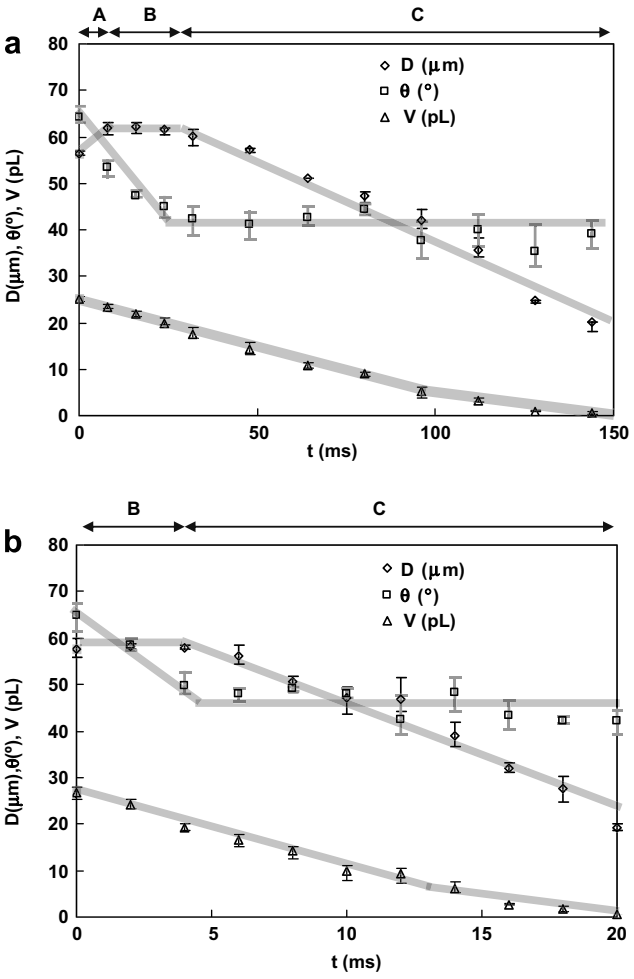

Fig. 12. Evaporation of the ethylene glycol droplet (about 38 μm of the droplet diameter) evaporating on a silicon substrate. (a) The silicon substrate temperature is 120 °C (EG-30-120 in Table 3). (b) The silicon substrate temperature is 160 °C (EG-30-160 in Table 3).

the equilibrium advancing angle (about 30° in Fig. 8) at room temperature. Positive $d\theta/dT$ was also observed [19,20], in support of the current experimental results. This result shows that the evaporation time scale (τ_{evap}) is larger than the spreading time scale in all conditions, but it can become comparable to the extra wetting time scale (τ_{wet}/κ) when the substrate temperature is high enough. Therefore, fluids such as highly viscous ethylene glycol with small equilibrium advancing angle, tend to exhibit extra wetting at low substrate temperatures. However, this extra wetting can be mitigated by substrate heating to improve the resolution of the printed dot.

4.2. Modeling of diffusion controlled evaporation for the droplet with a spherical cap

When the evaporation is slow enough for the temperature gradient in both droplet and substrate to be negligible, evaporation is controlled by the vapor diffusion in air and the governing equation in a spherical coordinate can be expressed as

$$\frac{\partial(rC)}{\partial t} = \mathscr{D}\frac{\partial^2(rC)}{\partial r^2} \tag{13}$$

Here, Δ, C, t, and r are diffusion coefficient, vapor concentration, time and radial distance in spherical coordinates, respectively. In Birdi's approach [21], the transient term in the above governing equation was neglected and by implementing the boundary condi-

tions $C = C_{sat}$ at $r = R$ and $C = C_\infty$ at $r \to \infty$, the vapor concentration and the evaporation rate ($\dot{m}$) for a hemispherical droplet on a flat surface were respectively obtained as follows:

$$C(r) = (C_{sat} - C_0)\frac{R}{r} + C_0 \tag{14}$$

$$\dot{m} = 2\pi R\mathscr{D}(C_s - C_\infty) \tag{15}$$

Here, C_{sat}, C_∞ and R denote the saturated vapor concentration, ambient vapor concentration and contact radius of the hemispherical droplet, respectively. Assuming that evaporation occurs while the contact angle is maintained at 90°, the temporal integration of the Eq. (15) gives the approximate total evaporation time as follows:

$$t_{evap} = \frac{\rho R^2}{2\mathscr{D}(C_{sat} - C_\infty)} \approx \frac{\rho D_0^2}{5\mathscr{D}(C_{sat} - C_\infty)} \tag{16}$$

It is thus seen that the evaporation time of the hemispherical droplet is proportional to the square of the original droplet diameter rather than the droplet volume.

When the contact angle is not 90°, the evaporation flux is not uniform along the air–fluid interface, so spherical symmetry does not hold. For example, when the contact angle is less than 90°, at the edge of the droplet interface, vapor can diffuse in the radial direction normal to droplet interface as well as in the outside direction, and as a result, evaporation is stronger near the contact line. Lebedev [22] and Picknett and Bexon [23] invoked an analogy between diffusive concentration fields and electro-static potential fields and derived an exact analytic solution for the vapor concentration field from the equivalent electrostatic potential field around the top half of an equiconvex lens. In addition, Hu and Larson [24] obtained a similar expression by fitting the result from a finite element method considering the edge effect as

$$\dot{m} = 2\pi R\mathscr{D}(C_{sat} - C_\infty)(0.135\theta^2 + 0.65), \tag{17}$$

where θ is the contact angle in radians. Eq. (17) yields Eq. (15) at contact angle of $\pi/2$. Based on the above expression (Eq. (17)), the evaporated volume is calculated for a small time interval and the new contact angle is obtained from Eq. (6) during the constant contact area phase. When the contact angle reaches the receding contact angle measured experimentally, the new contact radius is obtained in the same way. It is noted that the droplet temperature is assumed to equal to the initial substrate temperature throughout this process and the corresponding saturated vapor concentration is used for the calculation. This simplification would be reasonable if both thermal diffusion time scales inside the droplet ($\tau_{cond,f} \approx R^2/\alpha_f$) and silicon substrate ($\tau_{cond,s} \approx R^2/\alpha_s$) are much smaller than the total evaporation time ($t_{evap} \approx 0.2\tau_{evap}$). For the water droplet of 30 μm in radius at room temperature, the evaporation time scale is on the order of 10^{-1} s, while the thermal diffusion time scales of the droplet and silicon substrate are on the order of $10^{-3}$and 10^{-5} s, respectively. Therefore, the whole evaporation process would not be significantly affected by the above simplification. When the temperature is elevated, the evaporation time scale approaches the thermal conduction time scale inside the droplet, but the temperature field inside the droplet can be assumed uniform due to a strong Marangoni flow, so that the above simplification still holds. In relation, Ruiz and Black [25] compared the numerical results provided by solely considering the heat conduction to a model incorporating thermocapillary convection inside the droplet and showed that the heat conduction model underpredicted the evaporation rate due to the overpredicted temperature gradients. In addition, the advection effect due to moving substrate is also neglected in the present analysis, since the vapor diffusion time scale ($R^2/\mathscr{D}$) is very short compared to the advection time scale (R/u).

Fig. 13 shows the experimental results of water droplets of two different droplet diameters (42 μm for Fig. 13 (a) and 17.5 μm for

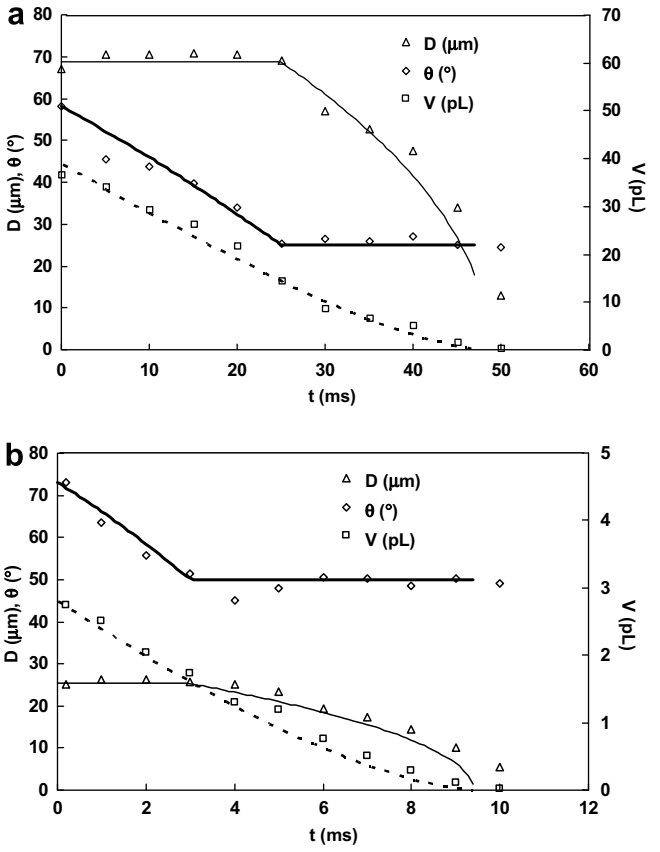

Fig. 13. The evolutions of contact diameter (D), contact angle (θ), and droplet volume of the evaporating water droplet on a silicon substrate at 70 °C. (a) Droplet diameter of 42 μm, (W-30-70 in Table 3) (b) Droplet diameter of 17.5 μm. (W-10-70 in Table 3) The theoretical curves are obtained by using Eq. (17) by dividing the constant contact area phase and the following constant contact angle phase and the initial contact angles and the receding angles for the calculation are obtained from the experimental measurement.

Fig. 13 (b)) at the silicon substrate temperature of 70 °C and the corresponding theoretical curves match well. Here, both the initial contact angle and receding angles measured experimentally and the ambient vapor concentration at 25 °C and 45% of relative humidity are used for C_∞. In addition, the diffusion coefficient of water vapor in air is obtained from reference [26]. The experimental results of the ethylene glycol droplets with initial droplet diameter of 36.5 μm and at silicon substrate temperature of 120 °C are

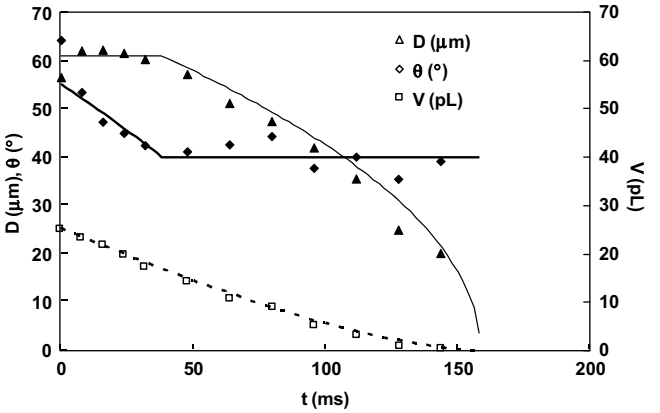

Fig. 14. The evolutions of contact diameter (D), contact angle (θ), and droplet volume of the evaporating ethylene glycol droplet on a silicon substrate at 120 °C (EG-30-120 in Table 3). The initial droplet diameter, the initial contact angle and the receding contact angle for calculation are set to 36.5 μm, 55° and 40°, respectively.

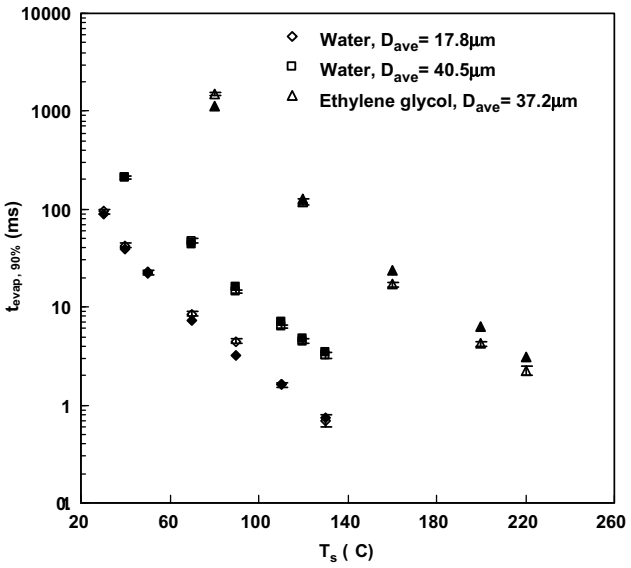

Fig. 15. The time required evaporating 90% volume ($t_{evap,90\%}$) of the water and ethylene droplet depending on the substrate temperature (T_s). The empty symbols and solid ones indicate the experimental results and the theoretical predictions, respectively.

shown in Fig. 14, which also shows good agreement with the corresponding theoretical curves. Here, the ambient vapor concentration is neglected, since the saturated vapor concentration at room temperature is less than 1% of that at 120 °C [26]. In addition, the diffusion coefficient of ethylene glycol is obtained from the correlation proposed by Chen and Othmer [27].

Fig. 15 shows the time elapsed for evaporating 90% of the initial droplet volume ($t_{evap, 90\%}$) with respect to varying temperature of the silicon substrate. In the case of water droplets of average diameters of 17.8 and 37.2 μm, the calculated evaporation time (marked by solid symbols) shows good agreement with the evaporation experimental results through the entire temperature range. The experimental evaporation time of ethylene glycol also agrees well with the calculated one, but the agreement is not as good as those of the water droplet, possibly because of the inaccurate vapor diffusion coefficient of ethylene glycol.

5. Concluding remarks

In this work, the spreading and evaporation phenomena of 2–70 pL droplets (i.e. 17–50 μm diameter) are studied experimentally. Fig. 16 gives an overview of the spreading and volume ratio evolution reconstructed from both our own and previous experimental and theoretical results. In this graph, different dimension-

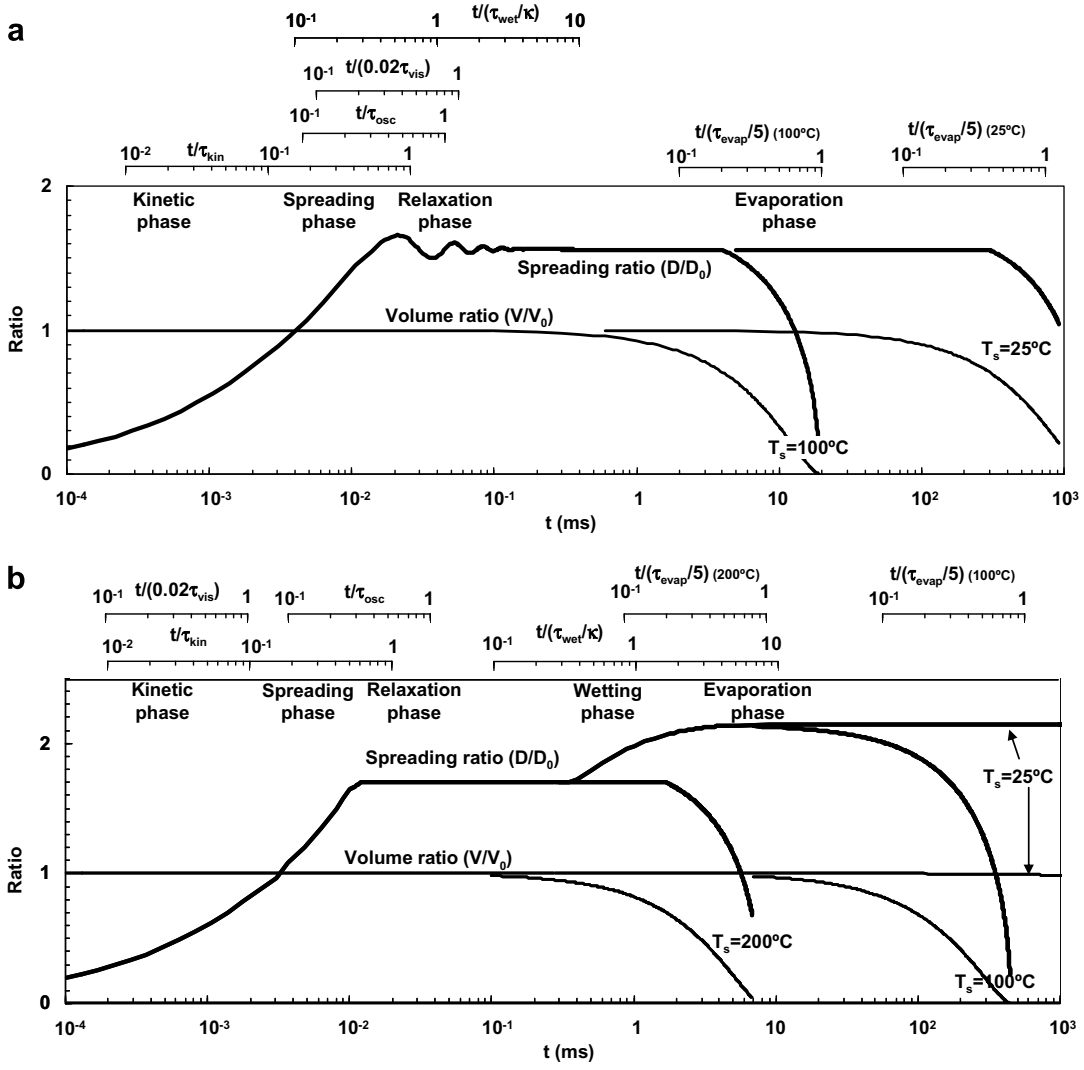

Fig. 16. Transient evolutions of spreading ratio and volume ratio of inkjet printed droplets. (a) Water droplet (b) Ethylene glycol. The thick solid line and the thin one represent the spreading ratio and the volume ratio, respectively.

less times are used for each phase, based on the modified time scales in Table 3. Note that according to these modified time scales, the transition between the inviscid and viscous regime can be obtained by setting the time scales equal. For example, equating the oscillation period and the damping time gives $\tau_{osc}/\tau_{vis} = 0.015$. In the same way, $\sqrt{\tau_{wet}/\tau_{vis}} = 0.0144$ and $\tau_{wet}/\tau_{osc} = 0.0138$. This indicates that the transition *Oh* should shift to 10^{-2}–10^{-1} [1], implying that the spreading phenomenon of the inkjet printed pico-liter droplet can be classified either in regime I or IV.

At the early stage of impact ($t/\tau_{kin} < 0.1$), the droplet spreading is dominated by the impact inertia and the evolution spreading ratio (β) depends only on t/τ_{kin}, as given in Eq. (3). Note that the center of the droplet does not contact the substrate surface at the end of the kinetic phase, so that this phase is very short compared to the whole spreading time. Then, the spreading phase follows ($0.1 < t/\tau_{kin} < 1 \sim 2$). In this phase, the evolution of β versus t/τ_{kin} depends on the fluid properties, such as viscosity, surface tension, contact angle, etc. In addition, the apparent dynamic advancing contact angle is significantly higher than the equilibrium advancing contact angle, which can be verified from Figs. 4 and 5 as well as Eq. (12). In the relaxation phase, the spreading ratio as well as droplet interface oscillates and this oscillation is damped out by viscous dissipation. Here, the oscillation period is approximately $\sqrt{\rho D_0^3/\sigma}$, and the relaxation phase is 3–4 times of the viscous damping time ($0.05\rho D_0^2/\mu$). Note that the oscillation periods of water and ethylene glycol are almost identical, but the viscous damping time of ethylene glycol is much smaller than that of water due to higher viscosity. Therefore, the oscillation after the spreading phase is almost absent in the ethylene glycol. While the spreading ratio does not change in the case of the water droplet after the relaxation phase, that of ethylene glycol increases with time. This extra wetting is driven by the uncompensated Young–Laplace force at the contact line resisted by either viscosity or inertia. Since τ_{wet}/κ is much bigger than τ_{osc} in the case of ethylene glycol, the surface tension driven extra wetting is controlled by the viscosity and the extra wetting data match well with theoretical predictions by Eq. (12). Note that in the case of the water droplet, τ_{wet}/κ is on the same order of τ_{osc}, so that the extra wetting phase cannot be seen after the relaxation phase.

Finally, evaporation occurs during $0.2\tau_{evap}$, which is longer than the other time scales at room temperature. As shown in Fig. 16, the volume ratio decreases in advance maintaining a constant contact area, and then both the volume ratio and the spreading ratio decrease with a constant contact angle. As the temperature of the droplet increases, the saturated vapor concentration increases significantly, and as a result, the evaporation time decreases sharply. In the case of water, even at 100 °C of the substrate temperature, the evaporation does not affect the spreading history, as shown in Fig. 16(a). However, in the case of highly viscous ethylene glycol, at 200 °C, $0.2\tau_{evap}$ is overlapped with τ_{wet}/κ, so that extra wetting can be mitigated. If the deposition material is suspended in the droplet, the resolution of the printed dots can be enhanced. It is noted that by elevating the substrate temperature, the early stage spreading evolution before evaporation in Fig. 16 changes due to temperature dependence of fluidic properties.

Acknowledgements

Financial support to Korea University by the Korea Research Foundation Grant funded by the Korean Government (MOEHRD) under Grant No. KRF-2006-331-D00044 and by the Korea University Grant and to University of California, Berkeley, by the U.S. National Science Foundation under Grant CTS-0417563 is gratefully acknowledged.

References

[1] S. Schiaffino, A.A. Sonin, Molten droplet deposition and solidification at low Weber numbers, Phys. Fluids 9 (1997) 3172–3187.
[2] R. Rioboo, M. Marengo, C. Tropea, Time evolution of liquid drop impact onto solid, dry surfaces, Exp. Fluids 33 (2002) 112–124.
[3] D.B. van Dam, C. Le Clerc, Experimental study of the impact of an ink-jet printed droplet on a solid substrate, Phys. Fluids 16 (2004) 3403–3414.
[4] B. Lavi, A. Marmur, The exponential power law: partial wetting kinetics and dynamic contact angles, Colloids Surf. A 250 (2004) 409–414.
[5] S. Chandra, C.T. Avedisian, On the collision of a droplet with a solid surface, Proc. R. Soc. Lond. A 432 (1991) 13–41.
[6] J. Madejski, Solidification of droplets on a cold surface, Int. J. Heat Mass Transfer 19 (1976) 1009–1013.
[7] W.J. Yang, Theory on vaporization and combustion of liquid drops of pure substances and binary mixtures on heated surfaces, Inst. Space Aeronautical Sci. 535 (1975) 423–455.
[8] J.D. Naber, Droplet Impingement on a Heated Surface, Ph.D. Thesis, University of Wisconsin, Madison, Wisconsin, 1992.
[9] B.L. Scheller, D.W. Bousfield, Newtonian droplet with a solid surface, J. AIChE 41 (1995) 1357–1367.
[10] M. Pasandideh-Fard, Y.M. Qiao, S. Chandra, J. Mostaghimi, Capillary effects during droplet impact on a solid surface, Phys. Fluid 8 (1996) 650–659.
[11] T. Mao, D.C.S. Kuhn, H. Tran, Spread and rebound of liquid droplets upon impact on flat surfaces, J. AIChE 43 (1997) 2169–2179.
[12] J. Chung, S. Ko, C.P. Grigoropoulos, N.R. Bieri, C. Dockendorf, D. Poulikakos, Damage-free low temperature pulsed laser printing of gold nanoinks on polymers, J. Heat Transfer 127 (2005) 724–732.
[13] Croucher, Design criteria and future-directions in inkjet ink technology, Ind. Eng. Chem. Res. 28 (1989) 1712–1718.
[14] J. Fukai, M. Tanaka, O. Miyatake, Maximum spreading of liquid droplets colliding with flat surfaces, J. Chem. Eng. Jpn. 31 (1998) 456–461.
[15] L.M. Hocking, On contact angles in evaporating liquids, Phys. Fluids 7 (1995) 2950–2955.
[16] T. Jiang, S. Oh, J.C. Slattery, Correlation for dynamic contact angle, J. Colloid Interf. Sci. 69 (1979) 74–77.
[17] S.F. Kistler, Hydrodynamics of Wetting, Wettability, Dekker, New York, 1993.
[18] S. Sikalo, Dynamic wetting angle of a spreading droplet, Exp. Thermal Fluid Sci. 29 (2005) 795–802.
[19] D.E. Sullivan, Surface tension and contact angle of a liquid-solid interface, J. Chem. Phys. 74 (1981) 2604–2615.
[20] S.G. Kandlikar, M.E. Steinke, Contact angles of droplets during spread and recoil after impinging on a heated surface, Trans. IChemE 79 (2001) 491–498.
[21] K.S. Birdi, D.T. Vu, A. Winter, A Study of the evaporation rates of small water drops placed on a solid-surface, J. Phys. Chem. 93 (1989) 3702–3703.
[22] N.N. Lebedev, Special Functions and Their Applications, Prentice-Hall, New Jersey, 1965.
[23] R.G. Picknett, R. Bexon, Evaporation of sessile or pendant drops in still air, J. Colloid Interf. Sci. 61 (1977) 336–350.
[24] H. Hu, R.G. Larson, Evaporation of a sessile droplet on a substrate, J. Phys. Chem. B 106 (2002) 1334–1344.
[25] O.E. Ruiz, W.Z. Black, Evaporation of water droplets placed on a heated horizontal surface, J. Heat Transfer 124 (2002) 854–863.
[26] D.R. Lide, CRC Handbook of Chemistry and Physics, 87th ed., Taylor and Francis, Boca Raton, 2007.
[27] N.H. Chen, D.F. Othmer, Net generalized equation for gas diffusion coefficient, J. Chem. Eng. Data 7 (1962) 37–41.